01 Aug 1995

Study of Interconnect Vias by the Discrete Surface Integral Method

Hao Shi

James L. Drewniak
Missouri University of Science and Technology, drewniak@mst.edu

Recommended Citation

H. Shi and J. L. Drewniak, "Study of Interconnect Vias by the Discrete Surface Integral Method," *Proceedings of the IEEE International Symposium on Electromagnetic Compatibility (1995, Atlanta, GA)*, pp. 228-233, Institute of Electrical and Electronics Engineers (IEEE), Aug 1995.
The definitive version is available at https://doi.org/10.1109/ISEMC.1995.523552

Study of Interconnect Vias by the Discrete Surface Integral Method

Hao Shi and James L. Drewniak
Electromagnetic Compatibility Lab
Department of Electrical Engineering
University of Missouri-Rolla
Rolla, Missouri, 65401

Abstract

A non-orthogonal time-domain full-wave solver, is developed based on the Discrete Surface Integral (DSI) technique. Closed form expressions are derived for the coefficients used in the leap-frog computation scheme so that the DSI technique can be implemented as a generalized finite-difference procedure. This procedure is employed to investigate the propagation characteristics of a typical interconnect via in printed circuits. The numerically calculated scattering parameters show consistent behavior with measured results. A square via with equal area is also evaluated.

1 Introduction

The finite difference time domain (FDTD) method is a powerful and conceptually straight forward technique for full-wave analysis of electromagnetic problems [1]. The conventional FDTD method handles complicated boundaries by staircasing with rectangular cells, which can lead to an excessive number of unknowns and inaccuracy. A number of non-orthogonal algorithms have emerged as an alternative approach to a problem involving a complicated arbitrary geometry. There are several types of time-domain non-orthogonal algorithms. One originates from tensor analysis [2, 3]. Another non-orthogonal algorithm suitable for implementation on an unstructured mesh is the Discrete Surface Integral (DSI) method [4]. By contrast with the conventional orthogonal Yee algorithm, a typical updating equation of the DSI method does not explicitly account for the contributions from the neighboring field components in terms of explicit coefficients. In this paper, an explicit formalism of the DSI method will be presented. This provides a rigorous mathematical approach for studying the DSI technique. Numerical dispersion, accuracy and stability of the DSI method applied in a 2D uniformly skewed mesh will also be discussed. A transient analytical solution is derived for a 3D rectangular waveguide excited with TE_{10} mode at one end and a matched load at the other end. A validation test is run on the waveguide problem with non-orthogonal mesh using the explicit DSI algorithm. Excellent agreement is observed between the simulated result and the analytical results. Finally, this explicit DSI formalism is applied to the study of the transmission characteristics of interconnect vias in printed circuits.

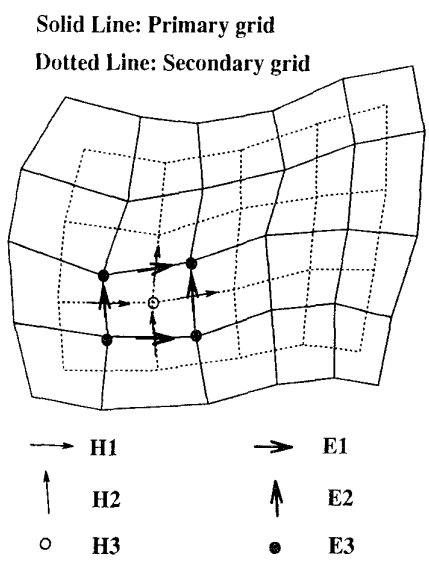

Figure 1: The primary and secondary grids in 2D.

2 An Explicit Formalism for the DSI Method

2.1 Fundamentals of the DSI method

In general, the DSI algorithm is applicable to an unstructured mesh where a piecewise linear approximation is employed to conform with any complicated geometry. The initial grid used to model the structure of interest is denoted the *primary grid*. A *centroid* of a cell is defined as the barycenter (center-of-mass) of its constituent vertices. Dual to the primary grid, a *secondary grid* is formed by connecting all the centroids of the primary mesh as nodes, (see Figure 1). The sampling locations for the electric field are at the centers of all edges in the primary mesh, while the sampling locations for the magnetic field are at the centers of all edges in the secondary mesh. There is a one-to-one correspondence between the edge/face in one grid and the face/edge in its dual grid. The DSI technique is developed by discretizing the two Maxwell curl equations. It has been shown that the two divergence equations are satisfied by this method in the sense that zero divergence of the time-advanced fields is locally preserved [4]. Exploiting the geometric duality between the grids, as well as the physical duality between the electric and magnetic

0-7803-2573-7/95/0000-0041 $4.00

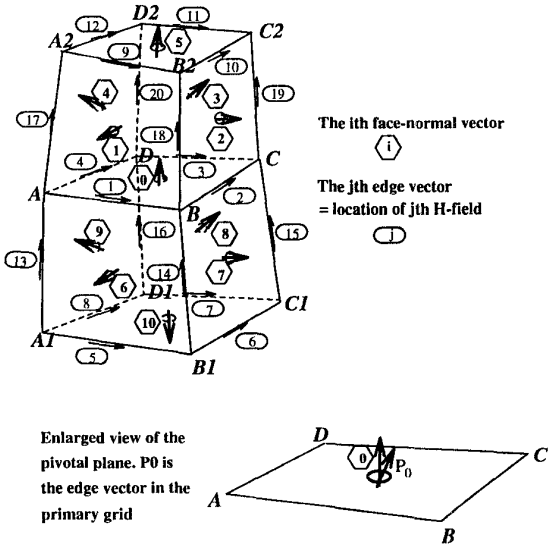

Figure 2: The two-cell model for the DSI algorithm.

fields, the DSI technique can be illustrated by discretizing the Ampere's law

$$\epsilon \int\int \frac{\partial \vec{E}}{\partial t} \cdot \hat{n} ds = \oint \vec{H} \cdot d\vec{l} \tag{1}$$

in the secondary grid.

Assume the electric field component is sampled along an edge in the primary grid with label No.0 shown in Figure 2. By mesh duality, this edge points to a face in the secondary grid, to which the same label No.0, can be assigned. Figure 2 has depicted the local environment of Face No.0 in the secondary grid. In the neighborhood of this pivotal location, each face is assigned a default positive normal direction, and each edge is given a default positive direction as well. The resultant two-cell model, with the attached labels will serve as a prototype.

Within the framework of the two-cell model, the discrete surface integration technique consists of the following steps:

Step 1: Application of Ampere's Law

First, the electric displacement current density, $\epsilon \frac{\partial \vec{E}}{\partial t} \equiv \vec{J}_d$, is chosen as the unknown vector. A preliminary estimate of $\vec{J}_d$ can be achieved by applying Ampere's law throughout all faces in the secondary grid. The resulting values are the $\vec{J}_d$ field projected along the directions normal to all faces in the secondary mesh, namely,

$$J_{d_\alpha} = \frac{1}{Area_\alpha} \sum_{\beta=1}^{4} H_{\alpha\beta} l_\beta, \tag{2}$$

where the $H_{\alpha\beta}$'s are associated with the βth edge centers around face α in the secondary mesh. As far as the field at the pivotal location is concerned, an improved approximation of the displacement current density will be based on the J_d values found associated with faces 0, 1, ..., 10 projected along their respective face normal directions, represented by the unit vectors $\vec{v}_0$, $\vec{v}_1$, ..., $\vec{v}_{10}$.

Step 2: Reconstruction of the Electric Displacement Current Density Vector

In general, the J_d quantities are values projected along the directions normal to all $\oint \vec{H} \cdot d\vec{l}$ loops, which in general are not coincident with the edge direction in the primary grid. Also, the results after Step 1 are too rough to give an accurate estimation of J_d. A procedure for reconstructing J_d at the face-center of the secondary grid and projecting to the primary grid is described below. First, the face-related J_d quantities are converted into vertex-related J_d quantities. Notice that in the upper cell (A-B-C-D&A2-B2-C2-D2), three faces 0, 4, and 1, share a common vertex, A, and a fictitious construct of $\vec{J}_{dA}$ is determined by solving the vector equations

$$\begin{cases} \vec{J}_{dAu} \cdot \vec{v}_0 = J_{d0} \\ \vec{J}_{dAu} \cdot \vec{v}_4 = J_{d4} \\ \vec{J}_{dAu} \cdot \vec{v}_1 = J_{d1}. \end{cases} \tag{3}$$

The subscript of $\vec{J}_{dAu}$ indicates that it is a $\vec{J}_d$ associated with vertex A of the *upper* cell. This intermediate $\vec{J}_d$ vector can be thought to be defined at vertex A. Similarly, $\vec{J}_{dBu}$, $\vec{J}_{dCu}$, and $\vec{J}_{dDu}$ bare similar meanings. This procedure is repeated in the lower cell (A-B-C-D&A1-B1-C1-D1) to determine $\vec{J}_{dAl}$, $\vec{J}_{dBl}$, $\vec{J}_{dCl}$, and $\vec{J}_{dDl}$.

Step 3: Averaging Scheme to Achieve $\vec{J}_d$ Associated with the Face-Center of the Secondary Grid

The vertex-related $\vec{J}_d$ values are then transformed into a vector associated with Face 0, by some reasonable weighted averaging scheme. Madsen has proposed three possible weighting schemes [5]. The weighting scheme adopted here is

$$\begin{aligned} &\vec{J}_{d0} = \\ &(\vec{J}_{dAu}(\vec{v}_0 \cdot \vec{v}_4 \times \vec{v}_1) + \vec{J}_{dBu}(\vec{v}_0 \cdot \vec{v}_1 \times \vec{v}_2) + \\ &\vec{J}_{dCu}(\vec{v}_0 \cdot \vec{v}_2 \times \vec{v}_3) + \vec{J}_{dDu}(\vec{v}_0 \cdot \vec{v}_3 \times \vec{v}_4) + \\ &\vec{J}_{dAl}(\vec{v}_0 \cdot \vec{v}_9 \times \vec{v}_6) + \vec{J}_{dBl}(\vec{v}_0 \cdot \vec{v}_6 \times \vec{v}_7) + \\ &\vec{J}_{dCl}(\vec{v}_0 \cdot \vec{v}_7 \times \vec{v}_8) + \vec{J}_{dDl}(\vec{v}_0 \cdot \vec{v}_8 \times \vec{v}_9))/ \\ &(\vec{v}_0 \cdot \vec{v}_4 \times \vec{v}_1 + \vec{v}_0 \cdot \vec{v}_1 \times \vec{v}_2 + \\ &\vec{v}_0 \cdot \vec{v}_2 \times \vec{v}_3 + \vec{v}_0 \cdot \vec{v}_3 \times \vec{v}_4 + \\ &\vec{v}_0 \cdot \vec{v}_9 \times \vec{v}_6 + \vec{v}_0 \cdot \vec{v}_6 \times \vec{v}_7 + \\ &\vec{v}_0 \cdot \vec{v}_7 \times \vec{v}_8 + \vec{v}_0 \cdot \vec{v}_8 \times \vec{v}_9). \end{aligned} \tag{4}$$

Step 4: Projection of Face Related $\vec{J}_d$ in the Secondary Grid onto the Corresponding Edge direction in the Primary Grid

The reconstructed $\vec{J}_{d0}$ associated with Face No.0 in the secondary grid is projected along the edge in the primary mesh, which is given simply by

$$J_{dP0} = \vec{J}_{d0} \cdot \vec{v}_{P0}, \tag{5}$$

where the subscript P0 in the edge vector implies that it is the edge vector with label "0" in the primary grid.

Step 5: Discretization in Time Using Central Differencing

Finally, the three indenpedent vector field components of the electric field (in primary grid) are finite-differenced in time as

$$\epsilon \frac{E_\alpha^{n+1} - E_\alpha^n}{\Delta t} = J_{dP0},$$

or

$$E_\alpha^{n+1} = E_\alpha^n + \frac{\Delta t}{\epsilon} J_{dP0}. \tag{6}$$

2.2 An Explicit Formalism for the DSI Method

Intuitively, the above five steps of the DSI suggest that the electric field at edge location Face No.0 (of the primary grid) is, in general, influenced by up to twenty magnetic field components defined at edges (of the secondary grid) 1 through 20 in the two-cell model. With the aid of MAPLE, a symbolic mathematical tool software developed by the University of Waterloo, the contribution from each of these twenty magnetic field components is extracted in terms of a coefficient with units $[length^{-2}]$. An explicit time-advancing equation for the electric field suitable for computer implementation is then given by

$$E_\alpha^{n+1} = \left(1+\frac{\sigma_\alpha}{2\epsilon_\alpha \Delta t}\right)^{-1} \times \left[(1-\frac{\sigma_\alpha}{2\epsilon_\alpha \Delta t})E_\alpha^n - \frac{\Delta t}{\epsilon_\alpha} J_\alpha^{n+1/2} + \frac{\Delta t}{\epsilon_\alpha}\sum_{\beta=1}^{\beta_{max}} t_{\alpha\beta} H_{\alpha\beta}^{n+1/2} l_{\alpha\beta}^s\right], \quad (7)$$

where the employed notations are:
α is the index of the field location,
σ_α, ϵ_α are average values of the conductivity and permeability,
β is the running index for neighboring edges in the secondary mesh,
$\beta_{\mathbf{max}}$ is 20 in general, and 4 for the orthogonal case,
$l_{\alpha\beta}^s$ are the lengths of the neighboring edges in the secondary mesh, and,
$\mathbf{t}_{\alpha\beta}$ are the coefficients representing contributions from all the surrounding H-field locations.
The twenty coefficients (α is dropped for simplicity, and $\beta = 1, 2, \cdots, 20$), are expressed in closed form. Using the labeling convention of the two-cell model and the following short hand notations —
(i) $\vec{v}_i$: the unit vector normal to the ith face;
(ii) $\vec{v}_{d0}$: the unit edge vector in the dual mesh, associated with the 0th face;
(iii) $V(0,i,j) \equiv \vec{v}_0 \cdot \vec{v}_i \times \vec{j}$;
(iv) $V(d0,i,j) \equiv \vec{v}_{d0} \cdot \vec{v}_i \times \vec{j}$;
(v) A_j: the area of the jth face; and,
(vi) the total weighting factor

$$\begin{aligned} W_{total} = {} & A_0[A_4A_1V(0,4,1) + A_1A_2V(0,1,2) \\ & + A_2A_3V(0,2,3) + A_3A_4V(0,3,4) \\ & + A_9A_6V(0,9,6) + A_6A_7V(0,6,7) \\ & + A_7A_8V(0,7,8) + A_8A_9V(0,8,9)]; \end{aligned}$$

— the twenty coefficients are then given by,

$$\begin{aligned} t_1 = {} & [A_4A_1V(d0,4,1) + A_1A_2V(d0,1,2) \\ & + A_2A_3V(d0,2,3) + A_3A_4V(d0,3,4) \\ & + A_9A_6V(d0,9,6) + A_6A_7V(d0,6,7) \\ & + A_7A_8V(d0,7,8) + A_8A_9V(d0,8,9) \\ & + A_0A_4V(d0,0,4) - A_0A_2V(d0,0,2) \\ & + A_0A_7V(d0,0,7) - A_0A_9V(d0,0,9)]/W_{total} \end{aligned}$$

$$\begin{aligned} t_2 = {} & [A_4A_1V(d0,4,1) + A_1A_2V(d0,1,2) \\ & + A_2A_3V(d0,2,3) + A_3A_4V(d0,3,4) \\ & + A_9A_6V(d0,9,6) + A_6A_7V(d0,6,7) \\ & + A_7A_8V(d0,7,8) + A_8A_9V(d0,8,9) \\ & + A_0A_1V(d0,0,1) - A_0A_3V(d0,0,3) \\ & - A_0A_6V(d0,0,6) + A_0A_8V(d0,0,8)]/W_{total} \end{aligned}$$

$$\begin{aligned} t_3 = {} & -[A_4A_1V(d0,4,1) + A_1A_2V(d0,1,2) \\ & + A_2A_3V(d0,2,3) + A_3A_4V(d0,3,4) \\ & + A_9A_6V(d0,9,6) + A_6A_7V(d0,6,7) \\ & + A_7A_8V(d0,7,8) + A_8A_9V(d0,8,9) \\ & - A_0A_4V(d0,0,4) + A_0A_2V(d0,0,2) \\ & - A_0A_7V(d0,0,7) + A_0A_9V(d0,0,9)]/W_{total} \end{aligned}$$

$$\begin{aligned} t_4 = {} & -[A_4A_1V(d0,4,1) + A_1A_2V(d0,1,2) \\ & + A_2A_3V(d0,2,3) + A_3A_4V(d0,3,4) \\ & + A_9A_6V(d0,9,6) + A_6A_7V(d0,6,7) \\ & + A_7A_8V(d0,7,8) + A_8A_9V(d0,8,9) \\ & - A_0A_1V(d0,0,1) + A_0A_3V(d0,0,3) \\ & + A_0A_6V(d0,0,6) - A_0A_8V(d0,0,8)]/W_{total} \end{aligned}$$

$$t_5 = A_0[A_9V(d0,0,9) - A_7V(d0,0,7)]/W_{total}$$

$$t_6 = A_0[A_6V(d0,0,6) - A_8V(d0,0,8)]/W_{total}$$

$$t_7 = t_5$$

$$t_8 = t_6$$

$$t_9 = A_0[A_2V(d0,0,2) - A_4V(d0,0,4)]/W_{total}$$

$$t_{10} = A_0[A_3V(d0,0,3) - A_1V(d0,0,1)]/W_{total}$$

$$t_{11} = t_9$$

$$t_{12} = t_{10}$$

$$\begin{aligned} t_{13} = {} & A_0[A_8V(d0,0,8) + A_7V(d0,0,7) \\ & - A_6V(d0,0,6) - A_9V(d0,0,9)]/W_{total} \end{aligned}$$

$$\begin{aligned} t_{14} = {} & A_0[A_9V(d0,0,9) + A_8V(d0,0,8) \\ & - A_7V(d0,0,7) - A_6V(d0,0,6)]/W_{total} \end{aligned}$$

$$\begin{aligned} t_{15} = {} & A_0[A_6V(d0,0,6) + A_9V(d0,0,9) \\ & - A_8V(d0,0,8) - A_7V(d0,0,7)]/W_{total} \end{aligned}$$

$$\begin{aligned} t_{16} = {} & A_0[A_7V(d0,0,7) + A_6V(d0,0,6) \\ & - A_9V(d0,0,9) - A_8V(d0,0,8)]/W_{total} \end{aligned}$$

$$\begin{aligned} t_{17} = {} & A_0[A_3V(d0,0,3) + A_2V(d0,0,2) \\ & - A_1V(d0,0,1) - A_4V(d0,0,4)]/W_{total} \end{aligned}$$

$$\begin{aligned} t_{18} = {} & A_0[A_4V(d0,0,4) + A_3V(d0,0,3) \\ & - A_2V(d0,0,2) - A_1V(d0,0,1)]/W_{total} \end{aligned}$$

$$\begin{aligned} t_{19} = {} & A_0[A_1V(d0,0,1) + A_4V(d0,0,4) \\ & - A_3V(d0,0,3) - A_2V(d0,0,2)]/W_{total} \end{aligned}$$

$$\begin{aligned} t_{20} = {} & A_0[A_2V(d0,0,2) + A_1V(d0,0,1) \\ & - A_4V(d0,0,4) - A_3V(d0,0,3)]/W_{total} \end{aligned}$$

The explicit algorithm has assumed the mesh to be structured, i.e., each node is uniquely assigned a triplet index (i,j,k), hence, it is a generalized FDTD scheme, in contrast with an unstructured mesh. When the mesh is orthogonal, the FDTD-DSI algorithm degenerates into the conventional Yee algorithm.

2.3 Numerical Dispersion and Stability of the DSI Method

An important advantage of having an explicit version of DSI algorithm is the feasibility of rigorously studying the numerical dispersion and stability properties of the algorithm. Theoretically, it is possible to get a closed form numerical dispersion relation for arbitrary local cell geometries. However, the immensely tedious algebra prevents a meaningful concise solution. For a two dimensional special case, where the grid is composed of uniform parallelogram cells, as shown in Figure 3, all t-coefficients can be simplified in terms of a few geometric parameters. Updating equations for all scalar components of electromagnetic fields can then be written. For example, the complete set of updating equations for the TE_z mode for two dimensional propagation are:

$$\begin{aligned}
&\frac{\partial E_1(i,j)}{\partial t}(\Delta l_1 \Delta l_2 \sin\theta_{12}) = \\
&\frac{1}{\epsilon}\{\Delta l_1[H_3(i,j) - H_3(i,j-1)] \\
&+\frac{1}{4}\cos\theta_{12}\Delta l_2[H_z(i-1,j) + H_z(i-1,j-1) \\
&-H_z(i+1,j) - H_z(i+1,j-1)]\} \qquad (8)
\end{aligned}$$

$$\begin{aligned}
&\frac{\partial E_2(i,j)}{\partial t}(\Delta l_1 \Delta l_2 \sin(\theta_{12})) = \\
&\frac{1}{\epsilon}\{\Delta l_2[H_3(i-1,j) - H_3(i,j)] \\
&+\frac{1}{4}\cos\theta_{12}\Delta l_1[H_3(i,j+1) + H_3(i-1,j+1) \\
&-H_3(i,j-1) - H_3(i-1,j-1)]\} \qquad (9)
\end{aligned}$$

$$\begin{aligned}
&\frac{\partial H_3(i,j)}{\partial t}(\Delta l_1 \Delta l_2 \sin\theta_{12}) = \\
&-\frac{1}{\mu}\{\Delta l_1[E_1(i,j) - E_1(i,j+1)] \\
&-\Delta l_2[E_2(i,j) - E_2(i+1,j)]\} \qquad (10)
\end{aligned}$$

where θ_{12} is the angle between the two unit vectors $\hat{x}_1$ and $\hat{x}_2$, and Δl_i (i=1,2) are the mesh dimensions along the two grid directions (Figure 3). An indexing method for computer implementation is used in the above three equations, whereby half integers are mapped into integers according to the rules shown in Table 1.

For a plane wave with propagation vector $\vec{\beta}$ and frequency ω, propagating through the uniform grid, a time-harmonic solution for all field components can be expressed as

$$\begin{Bmatrix} E_1(i,j,k) \\ E_2(i,j,k) \\ H_3(i,j,k) \end{Bmatrix} = \begin{Bmatrix} E_{10}(i,j,k) \\ E_{20}(i,j,k) \\ H_{30}(i,j,k) \end{Bmatrix} e^{J(\omega t - \vec{\beta}\cdot\vec{r})} \qquad (11)$$

where $J \equiv \sqrt{-1}$, $\vec{r} = i\Delta l_1\hat{x}_1 + j\Delta l_2\hat{x}_2 + k\Delta l_3\hat{x}_3$, and $\vec{\beta} = \beta_1\hat{x}_1 + \beta_2\hat{x}_2 + \beta_3\hat{x}_3$. Also, $t = n\Delta t$ and $\beta_3 = 0$ for the 2D problem. Upon inserting the presumed solutions (11) into the updating equations (8), (9), and (10), the result can be cast into a set of homogeneous linear simultaneous equations with unknowns $\{E_{x0}, E_{y0}, H_{z0}\}$. Since trivial solutions are not acceptable, the secular determinant should vanish, which, in turn, results in an equation relating ω to k — a discrete dispersion relation. When the following substitutions are made in the notation,

$\|\vec{\beta}\| \to$ k	the wave number
$\hat{x}_1, \hat{x}_2 \to \xi, \eta$	the basis vectors
$\Delta l_1, \Delta l_2 \to \Delta\xi, \Delta\eta$	the spatial increments
$\theta_{12} \to \theta$	angle between the basis vectors
$\vec{\beta}\cdot\hat{\xi} \to$ k $\cos\phi$	ϕ is the propagation angle w.r.t. $\hat{\xi}$

and observing that

$$\frac{\beta_1}{\sin(\theta-\phi)} = \frac{\beta_2}{\sin\phi} = \frac{k}{\sin(\pi-\theta)}$$

as seen in Figure 3, then

$$\begin{aligned}
\beta_1 + \beta_2\cos\theta &= k\cos\phi \\
\beta_2 + \beta_1\cos\theta &= k\cos(\phi-\theta)
\end{aligned}$$

the dispersion relation is simplified to

$$\begin{aligned}
&\frac{1}{(c\Delta t)^2}\sin^2\left(\frac{\omega\Delta t}{2}\right) \\
&= \frac{1}{\sin^2}\left\{\frac{1}{\Delta\xi^2}\sin^2\left(\frac{k\Delta\xi\cos(\phi)}{2}\right)\right. \\
&+\frac{1}{\Delta\eta^2}\sin^2\left(\frac{k\Delta\eta\cos(\phi-\theta)}{2}\right) - \frac{\cos\theta}{2\Delta\xi\Delta\eta} \\
&\left.\sin(k\Delta\eta\cos(\phi))\cdot\sin[k\Delta\eta\cos(\phi-\theta)]\right\}, \qquad (12)
\end{aligned}$$

which is identical to that reported by Ray [6].
Two interesting consequencies of (12) are:
(i) When both Δl_1 and Δl_2 approach zero, the continuous dispersion relation is retrieved, i.e. $\omega = c\cdot k$. Further, applying a series expansion over small arguments (Δt, Δl_1,

Table 1: The mapping of programming indices into physical indices

	Programming	Physical
E_1	(i,j,k)	(i+1/2,j,k)
E_2	(i,j,k)	(i,j+1/2,k)
E_3	(i,j,k)	(i,j,k+1/2)
H_1	(i,j,k)	(i,j+1/2, k+1/2)
H_2	(i,j,k)	(i+1/2,j,k+1/2)
H_3	(i,j,k)	(i+1/2,j+1/2,k)

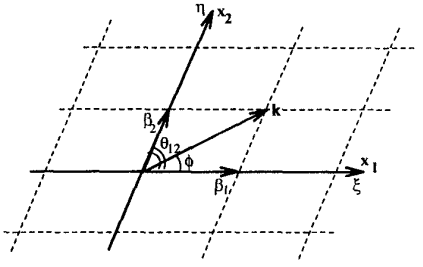

Figure 3: The wave vector in skewed uniform grid.

Δl_2) the DSI algorithm can be shown to be second order accurate in both space and time, for the 2D uniformly skewed mesh.
(ii) The stability criterion for the special case of a 2D uniformly skewed mesh shown in Figure 3 is:

$$c\Delta t \leq \frac{\sin(\theta)}{\sqrt{\Delta\xi^{-2} + \Delta\eta^{-2}}} \tag{13}$$

In addition to a Courant factor similar to that for the orthogonal algorithm, the DSI method for a 2D uniform grid is also dependent on $\sin\theta$. Thus, it is preferable to make the skew angle as close to 90° as possible in order to avoid unnecessarily small time steps.

3 Simulation of Vias with the DSI Method

The described FDTD-DSI scheme is implemented on an HP-9000 series computer. Validation test is carried out by analyzing the propagation of the dominant TE_{10} mode in a three dimensional rectangular waveguide. The dimensions of the waveguide are $a = 21.868mm$ for the broad wall, $b = 10.934mm$ for the narrow wall, and $L = 248.5mm$ for the total length. An orthogonal grid is constructed with $\Delta x = \Delta y = \Delta z = \Delta = 0.994mm$. A non-orthogonal grid is created by replacing a portion of the orthogonal grid with skewed segments, such that the surface of a circular cylinder ($D = 6.5mm$, located at the center along the longitudinal direction, a cross-section view on the broad wall is a circle) is conformed by piecewise linear approximation. The waveguide is excited at the near end (z=0), with $E_y|_{z=0} = f(t)\sin(\pi\frac{x}{x_{max}})$ and $f(t) = \sin(2\pi f_0 t)(e^{-\beta(f_0 t-1)^2 - e^{-\beta}})/(1-e^{-\beta})$ with $f_0 = 12GHz$ and $\beta = 1$. Matched boundary conditions are applied at the far end (z=L). An analytical solution is obtained for $\pi L/x_{max} >> 1$:

$$E_y(x,y,z;t) = \{f(t-\tau) - f(t)* \\ (u(t-\tau)\frac{\omega\tau}{t^2-\tau^2}J_1(\omega\sqrt{t^2-\tau^2}))\}\sin(\pi\frac{x}{x_{max}}); \tag{14}$$

where $J_1()$ is the Bessel function of order one, "*" represents convolution, and $\omega = \frac{c}{x_{max}}$ is the cutoff angular frequency of the TE_{10} mode. Time histories ($\Delta t = 0.596ps$) of E_y at location ($x = 12\Delta$, $y = 6\Delta$, $z = 80\Delta$) are collected for both the convetional Yee algorithm on the orthogonal mesh and the FDTD-DSI algorithm on the non-orthogonal mesh. The time series predicted by equation (14) is calculated by MATLAB. Figure 4 has shown that the FDTD-DSI result on a non-orthogonal mesh agrees well with the results found by the analytical solution, and by the conventional orthogonal FDTD method on a comparable rectangular grid.

The FDTD-DSI method is used to study via interconnects in multilayer printed circuits. A typical via is considered for which experimental results are available [7]. As shown in Figure 5(a), the via contains a cylindrical metal wall linking pads in two traces on different levels. The width of both traces is 3.3 mm, the diameter of the circular landing pad is 3.9 mm, and the diameter of the through-hole is 0.7 mm. The two conducting traces are separated

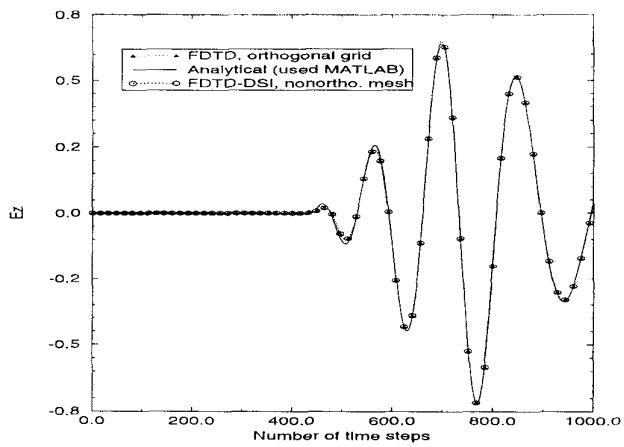

Figure 4: The time-domain results of the validation test.

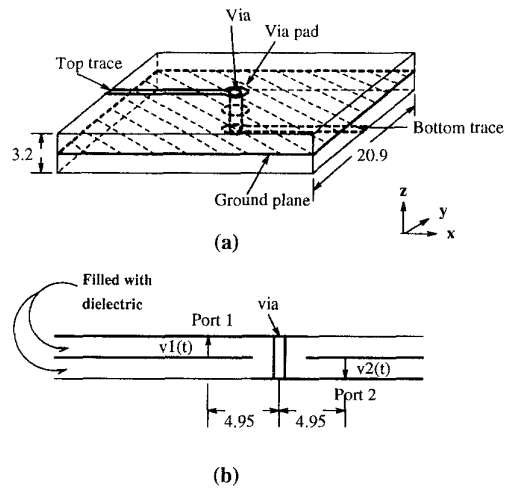

Figure 5: The geometry of the via board (All dimensions are in millimeters).

by a dielectric ($\epsilon_r = 3.4$) and a ground plane. The ground plane leaves a clearance hole with a diameter of 3.9 mm in the vicinity of the via. The computational domain is extended invariantly along the z-direction from a non-orthogonal two-dimensional mesh in the xy-ground plane. The cell thickness along the z-direction is homogeneously 0.8 mm. A top view of the mesh in the xy-plane is shown in Figure 6. The grid conforms with the geometries of all structures with piecewise linear segments. The center ground plane coincides with the center plane of the grid. Two layers of cells are filled between the trace planes and the ground plane. The distance between the lower/upper trace plane and the lower/upper domain wall is three cell lengths. The computational domain is terminated with perfect electric conducting (pec) walls on the four sides, and first order Mur absorbing boundary conditions on the two ends. A pseudo-Gaussian pulse is launched under the top trace near Port 1 by enforcing a quasi-TEM spatial distribution for E_z, the electric field component perpendicular to the conducting strips. The time dependence is given by $f(t) = (e^{-\beta(f_0 t-1)^2 - e^{-\beta}})/(1-e^{-\beta})$ with $f_0 = 20GHz$ and $\beta = 10$. The pulse propagates along +x direction. The electric field component parallel with the strip, E_y at

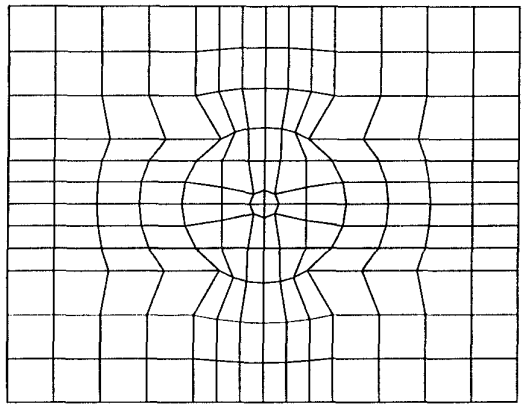

Figure 6: The 2D mesh (the non-orthogonal portion) for modeling the via.

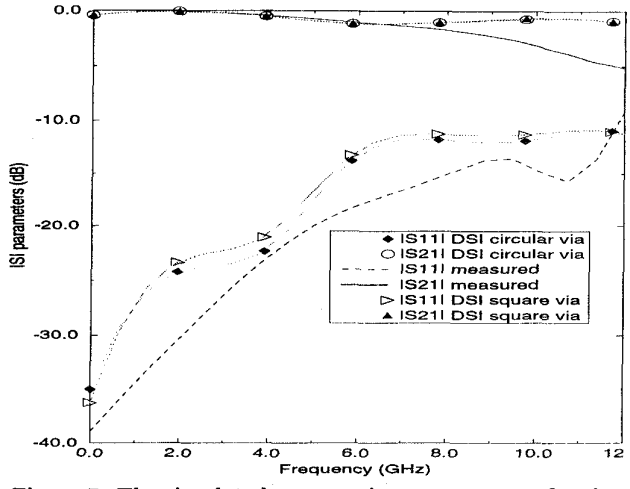

Figure 7: The simulated propagation parameters of a via.

the excitation end is computed by first order Mur ABCs. Once the pulse is completed, first order Mur Absorbing Boundary Conditions (ABCs) are utilized in the source plane. An ABC wall is always applied at the terminating end. The voltage signal is obtained by integrating the electric field between the trace and the center ground plane, and the choice for sampling ports (see Figure 5(b)) are chosen in order to compare with the published measured data [7]. The time increment is 0.28 ps.

The S-parameters are computed from the FFT of reflected and transmitted waves using a reference incident wave on the top trace only without the via and terminated in a matched boundary. The S-parameters are then computed by

$$\begin{aligned} |S_{11}(\omega)| &= [\tilde{V}_{port1} - \tilde{V}_{ref}]/\tilde{V}_{ref} \\ |S_{21}(\omega)| &= \tilde{V}_{port2}/\tilde{V}_{ref} \end{aligned} \tag{15}$$

where $\tilde{V}$ is the (Discrete) Fourier transform of $V(t)$. The computed $|S_{11}|$ and $|S_{21}|$ are compared with the measured results by Maeda *et al.* in Figure 7, [7]. The $|S_{11}|$ curve agrees with the experimental data within 5 dB, while the $|S_{21}|$ curve agrees with the experimental data within 0.1 dB for frequencies below 7 GHz. Due to the pec side walls employed to truncate the mesh, waveguide modes are excited for frequencies higher than 7.2 GHz, the cutoff frequency of the dominant TE_{10} mode. Thus, the simulated results are limited to frequencies below 7.2 GHz, however, the modeled results are plotted up to 12 GHz. The waveguide structure generates unphysical scattering, and is believed to be one of the main sources of the discrepancies. Other sources of error include the relatively severe skewness of the grid in the vicinity of the via, and the imperfect end matching conditions when first order ABCs are applied at both ends.

To investigate the possible effect of curvature of the circular shaped via, a square via with equal area is also modeled under the same conditions. The calculated S-parameters are displayed in Figure 7. The S-parameters for the square via deviate at most 1.0 dB from those of the circular via.

References

[1] K. S. Yee, "Numerical solution of initial boundary value problems involving Maxwell's equations in isotropic media," *IEEE Transactions on Antennas and Propagation*, vol. 14, pp. 302–307, 1966.

[2] R. Holland, "Finite-difference solution of maxwell's equtions in generalized nonorthogonal coordinates," *IEEE Transactions on Nuclear Science*, vol. 30, pp. 4589–4591, 1983.

[3] J.-F. Lee, R. Palandech, and R. Mittra, "Modeling three-dimensional discontinuities in waveguides using nonorthogonal FDTD algorithm," *IEEE Transactions on Microwave Theory and Techniques*, vol. 40, pp. 346–352, 1992.

[4] N. K. Madsen, "Divergence preserving discrete surface integral methods for Maxwell's curl equations using non-orthogonal unstructured grids," *Lawrence Livermore National Laboratory Technical Report UCRL-JC-109787*, 1992.

[5] N. K. Madsen and R. W. Ziolkowski, "Numerical solution of Maxwell's equations in the time domain using irregular nonorthogonal grids," *Wave Motion*, vol. 10, pp. 583–596, 1988.

[6] L. Shlager, J. G. Maloney, S. L. Ray, and A. F. Peterson, "Relative accuracy of several finite-difference time-domain methods in two and three dimensions," *IEEE Transactions on Antennas and Propagation*, vol. 41, pp. 1732–1737, 1993.

[7] S. Maeda, T. Kashiwa, and I. Fukai, "Full wave analysis of propagation characteristicsof a through hole using the finite-difference time-domain method," *IEEE Transactions on Microwave Theory and Techniques*, vol. 39, pp. 2154–2159, 1991.